Analytical and Bioanalytical Chemistry
https://doi.org/10.1007/s00216-019-01765-7

RESEARCH PAPER

Enhanced photoelectrochemical sensing based on novel synthesized Bi_2S_3@Bi_2O_3 nanosheet heterostructure for ultrasensitive determination of L-cysteine

Feng Xia Wang[1] · Cui Ye[1] · Shi Mo[2] · Hong Qun Luo[1] · Jing Rong Chen[1] · Yan Shi[1] · Nian Bing Li[1]

Received: 6 December 2018 / Revised: 23 February 2019 / Accepted: 6 March 2019

Abstract

The design of a low-cost and highly efficient photoactive heterojunction material for sensing is still a challenging issue. On the basis of the formation of sheet-like Bi_2O_3 via coating Bi_2S_3, a novel Bi_2O_3@Bi_2S_3 heterostructure is controllably synthesized via a facile water bath approach. The prepared Bi_2O_3@Bi_2S_3 nanosheets show a superior photoelectrochemical (PEC) performance for the detection of L-cysteine (L-Cys), and the photocurrent signal is three and four times higher than those of Bi_2S_3 and Bi_2O_3 under visible irradiation, respectively. Also, the heterostructure presents an outstanding linear range for the detection of L-Cys: 0.1–10,000 μM. In addition, the mechanism of improved PEC response of Bi_2O_3@Bi_2S_3 nanosheets is investigated according to the estimated energy band positions. Thus, the integration of the novel heterostructure and the photoelectrochemical technique demonstrates a rapid photocurrent response, showing a great effect on the performance of the sensing system and a new PEC method for highly selective and sensitive chemical detection.

Keywords Biosensor · Photoelectrochemistry · Cysteine · Bi_2O_3@Bi_2S_3 heterojunction

Introduction

L-Cysteine (L-Cys) is a fundamental material to build up the functional parts of many proteins and enzymes, thus playing a very important role in some biological fields. L-Cys has been widely used in the field of pharmaceutical and clinical diagnoses and food processes [1]. The level of L-Cys is closely related to the symptoms of the disease, including skin lesions, children slow growth, lethargy, hypoglycemic brain damage, hair depigmentation, loss of muscle and fat, and weakness [2]. Therefore, it is of great importance to develop a sensitive and selective assay to detect L-Cys. It has been reported that different analytical methods have been used to detect L-Cys, such as high-performance liquid chromatography (HPLC) [3], colorimetry [4], electrochemiluminescence (ECL) [5], and some electrochemical methods [6, 7]. Compared with these traditional detection methods, the photoelectrochemical (PEC) method owns low background signal, simple operation and condition, low cost, and high sensitivity [8–11]. Additionally, the integration of PEC method with bioanalysis has inaugurated an innovative methodology for the study of biological analytes, such as bacteria, small molecules, macromolecules, and cells [12, 13].

Ever since Edmond Becquerel discovered the photoelectric effect, the emerged PEC bioanalysis has been endowed with incredible merits, owing to the merits of low cost, high sensitivity, plain instrumentation, and robustness [14–16]. It is worth noting that the photoactive materials can furthest ensure the PEC bioanalysis performance for its sufficient carrier transport properties and efficient light harvest ability [8, 17, 18]. Up to now, SnO_2, TiO_2, g-C_3N_4, CdS quantum dot, and other semiconductor materials have been developed as photoactive materials, and the choice of such materials plays a key role in the design of PEC sensor [19–22]. In various

Electronic supplementary material The online version of this article (https://doi.org/10.1007/s00216-019-01765-7) contains supplementary material, which is available to authorized users.

✉ Hong Qun Luo
luohq@swu.edu.cn

✉ Nian Bing Li
linb@swu.edu.cn

[1] Key Laboratory of Eco-environments in Three Gorges Reservoir Region (Ministry of Education), School of Chemistry and Chemical Engineering, Southwest University, Chongqing 400715, China

[2] Department of Physics, City University of Hong Kong, Tat Chee Avenue, Kowloon 999077, Hong Kong, China

Published online: 27 March 2019

kinds of photoactive materials, metal oxide is a typical kind used in PEC devices [23]. Due to the good photostability in acidic condition [24, 25], low cost, and favorable direct band gap, bismuth trioxide (Bi_2O_3) has been considered as a type of alternative photoactive material and can be used in sensor, photovoltaic field, and catalysis [26–28]. Moreover, Bi_2O_3 shows a 2.5–2.8-eV direct band gap, which can serve as a photocatalyst driven by visible light and the valence band maximum (VBM) of Bi_2O_3 is 3.13 eV. This phenomenon makes it positive enough to provide potential for oxygen due to its strong oxidizing power. What is more, the varieties of crystal structures of Bi_2O_3 endow it with the semiconductor properties of p-type or n-type, which makes it be widely used in some fields [29]. However, the poor harvesting of solar energy and the low activity of photocatalytic and charge carrier separation of pure Bi_2O_3 result in the unsatisfactory PEC photocurrent response.

Compared with the single component photoactive materials, more and more attentions have been paid to heterogeneous photoactive materials [30–32], among which, the p-n heterojunctions are widely studied because of their effective photoexcited charge separation efficiency and high solar energy efficiency, which can be formed via an inner electric field between the p-type and n-type semiconductors [33]. Thus, in order to enhance the PEC performance of Bi_2O_3, coupling pure Bi_2O_3 with other semiconductors to construct a heterojunction is necessary. Fortunately, bismuth sulfide (Bi_2S_3) has a direct band gap (1.3–1.7 eV) [34], which can fully make use of visible light, and its applications as electrochemical hydrogen storage [35], biomolecule detection [36], hydrogen sensors [37], and photoresponsive materials have also been reported. In recent years, Bi_2S_3 appears to be a sensitizer for the good absorption capacity so that it can absorb wide-spectrum light irradiation (up to 800 nm) [38]. Inspired by the enhanced PEC performance and the improved electron hole pair transfer in heterostructure samples, a Bi_2O_3@Bi_2S_3 heterostructure was designed and applied to the L-Cys sensing. The as-prepared Bi_2O_3-modified Bi_2S_3 nanosheets demonstrated an enhanced photocurrent response for L-Cys assay.

As is known, there is no report focusing on Bi_2O_3@Bi_2S_3 heterostructure for the construction of PEC sensing of L-Cys up to now. This Bi_2O_3@Bi_2S_3 heterostructure was synthesized through an easy water bath approach. As a proof-of-concept, the Bi_2O_3@Bi_2S_3 heterostructure was considered as the photoactive material to establish a PEC sensing for the determination of L-Cys. It should be noticed that L-Cys can be ligated onto the substrate with the help of gold nanoparticles (GNPs), through forming covalent bonds of Au-S between the sulfydryl of L-Cys and GNPs, and thus further oxidized by the hole from Bi_2S_3. Additionally, the thin conducting layer makes the electron transfer to the Bi_2S_3 surface more quickly. Therefore, the photocurrent signal enhancement is significant. The heterojunction structure designed in this way has good synergistic effect; therefore, it can promote the charge transfer, inhibit the recombination of electron hole pairs, and thus improve the experimental performance for L-Cys detection. The schematic diagram of the Bi_2O_3@Bi_2S_3-based sensor and assay principle for the determination of L-Cys during the preparation are shown in Scheme 1. As mentioned above, the sensing process of Bi_2O_3@Bi_2S_3 for the L-Cys assay under visible light demonstrates an outstanding activity compared with that of pure Bi_2O_3 or Bi_2S_3. The energy band positions were calculated in this work and the mechanism of enhanced PEC response for the Bi_2O_3@Bi_2S_3 nanosheets was investigated in detail.

Experimental section

Materials and reagents

All the amino acids used including L-arginine (L-Arg), L-proline (L-Pro), L-alanine (L-Ala), L-histidine (L-His), L-tryptophan (L-Try), L-leucine (L-Leu), L-threonine (L-Thr), L-serine (L-Ser), L-cysteine (L-Cys), and L-glutamic acid (L-Glu) were purchased from Sigma-Aldrich (St. Louis, MO). Glutathione (GSH), hexadecyl trimethyl ammonium bromide (CTAB), bismuth nitrate (Bi $(NO_3)_3 \cdot 5H_2O$), nitric acid (HNO_3, 14 M), and thioacetamide (TAA) were purchased from Sigma-Aldrich (St. Louis, MO). All of the other reagents were of analytical grade and used without further purification. Ultrapure water used throughout the work was prepared by a water purification system (18.2 MΩ cm).

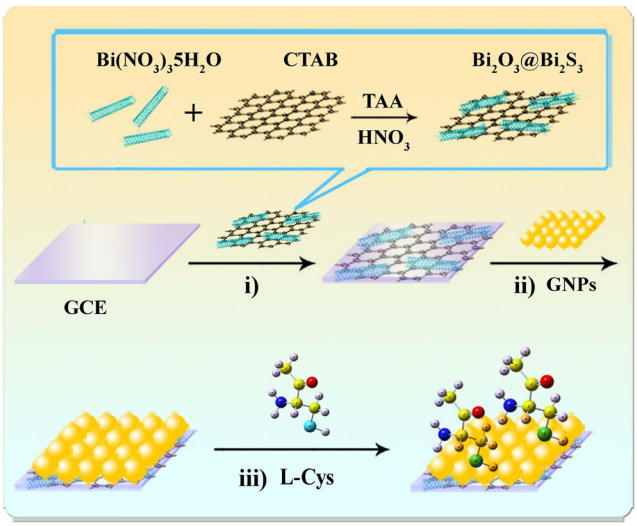

Scheme 1 Schematic representation for the preparation process of the PEC sensor for L-Cys assay

Characterizations

An XRD-7000 was used to record the X-ray diffraction (XRD) patterns at a scanning rate of 2° min^{-1} from 10 to 80° (Shimadzu, Japan). A JEM-2100 field emission scanning electron microscope (FESEM) equipped with a field emission gun (FEG) at 200 kV on JEOL-7800F was used to characterize the morphology of the prepared samples, and the energy-dispersive X-ray spectroscopy (EDS) measurement was conducted on an INCA X-Max 250 (Japan Electron Optics Laboratory Co., Japan). The transmission electron microscopy (TEM) image was recorded on a JEM-2100 equipped with a field emission gun (FEG) at 200 kV (TEM, JEOL-2100, Japan). X-ray photoelectron spectroscopy (XPS) analysis was carried out on a Thermo ESCALAB 250Xi spectrometer (Thermoelectricity Instruments, USA) with Al Ka X-ray (1486.6 eV) as the light source. UV-vis diffuse reflectance spectra (UV-vis DRS) were conducted using a Varian Cary 300 spectrometer equipped with an integrating sphere (Shimadzu Co., Japan). A super digital thermostat bath of SD-101-005DB was used to maintain the experiment temperature (Sida Experimental Equipment Ltd., China). CHI 660B electrochemical workstation (Shanghai Chenhua Instruments Co., China) was utilized for electrochemical and PEC measurements. Visible light irradiation was carried out on a CHF-XM35-500W Xenon lamp parallel light source system, equipped with a white light transmissions filter (Beijing Trusttech Co. Ltd., China). Three-electrode cell was used at room temperature, in which a saturated calomel electrode (SCE), a platinum wire, and a modified glassy carbon electrode (GCE, $\Phi = 3$ mm) were used as the reference electrode, the counter electrode, and the working electrode, respectively, for PEC measurements or electrochemical measurements. The geometric area of the GCE obtained by electrochemical measurements is approximately 9.6 mm^2 (see Electronic Supplementary Material (ESM) Fig. S1).

Synthesis of Bi_2S_3@Bi_2O_3 heterojunction

The samples were synthesized by the water bath approach according to the literature with minor modification [39]. To prepare the Bi_2S_3@Bi_2O_3 heterojunction, 125 μL of HNO_3 (14 M) was mixed with ultrapure water (5 mL) under the stirring condition at first, and then a portion of 0.2332 g of $Bi(NO_3)_3{\cdot}5H_2O$ was added to the HNO_3 solution above and the milky white solution was formed under intense agitation and marked as A solution. Afterwards, CTAB (0.1248 g) and TAA (0.0698 g) were added to ultrapure water (60 mL) to obtain the sulfurization agent solution under ultrasonication, which was labeled as B solution. Subsequently, A solution was dropwise added to B solution. The mixture was water-bathed at 30 °C for 180 min and was then washed with absolute alcohol and ultrapure water alternately via centrifugation. For comparison, pure Bi_2S_3 was also synthesized using the water bath approach under the same conditions except that a higher amount of TAA was used (0.380 g). When TAA is not used in the synthesis process, Bi_2O_3 nanosheets can be prepared. For the preparation of the colloidal GNPs, 38.8 mM sodium citrate was utilized to reduce $HAuCl_4$ (1 wt%) at 100 °C for half an hour.

Preparation of electrodes

Commercialized GCE was used in this study. The GCE surface was of 3 mm × 3 mm in size. The GCE surface was first polished on chamois leather using 0.5 and 0.05 μM alumina slurry and sonicated in anhydrous ethanol and ultrapure water bath. After this step, the cleaned GCE was modified using the Bi_2S_3@Bi_2O_3 nanosheets (7 μL, 1.5 mg/mL) and evaporated in air. In the process of the experiment, the sample was dissolved in ultrapure water to prepare 1.5 mg/mL Bi_2S_3@Bi_2O_3, and a uniformly distributed suspension was formed after 10 min ultrasonic dispersion. The modified electrode in this step was denoted as Bi_2S_3@Bi_2O_3/GCE and worked as the sensing substrate. Furthermore, the Bi_2S_3@Bi_2O_3/GCE electrode was incubated with GNPs (10 μL) at room temperature for 2 h, followed by rinsing and drying; then, the electrode was marked as GNPs/Bi_2S_3@Bi_2O_3/GCE, and stored in a refrigerator when not in use.

PEC detection for L-Cys

The PEC curves of L-Cys were recorded in the 4 mL detection cell. The GNPs/Bi_2S_3@Bi_2O_3/GCE was dipped in various concentrations of L-Cys (10 μL) for 20 min, ensuring that the L-Cys was ligated onto the substrate based on the formation of Au-S covalent bond between the sulfydryl of L-Cys and GNPs. The final prepared electrode was abbreviated as L-Cys/GNPs/Bi_2S_3@Bi_2O_3/GCE. The photocurrent response of the L-Cys/GNPs/Bi_2S_3@Bi_2O_3/GCE was measured with a CHI 660B electrochemical workstation in a conventional three-electrode system in 0.1 M Na_2SO_4 solution by applying a bias potential of 0.2 V.

Results and discussion

Characterizations of materials

The microscopic structures of the prepared Bi_2O_3 and Bi_2S_3@Bi_2O_3 heterojunction were characterized using the FESEM. Figure 1 A shows the typical morphology of Bi_2O_3 with a lamellar-like structure. Figure 1 B displays the high-magnification image of Bi_2O_3 nanosheets, and the nanosheets are smooth and neat. The prepared Bi_2S_3@Bi_2O_3 nanosheets in Fig. 1 C illustrate that the surface of the sample becomes

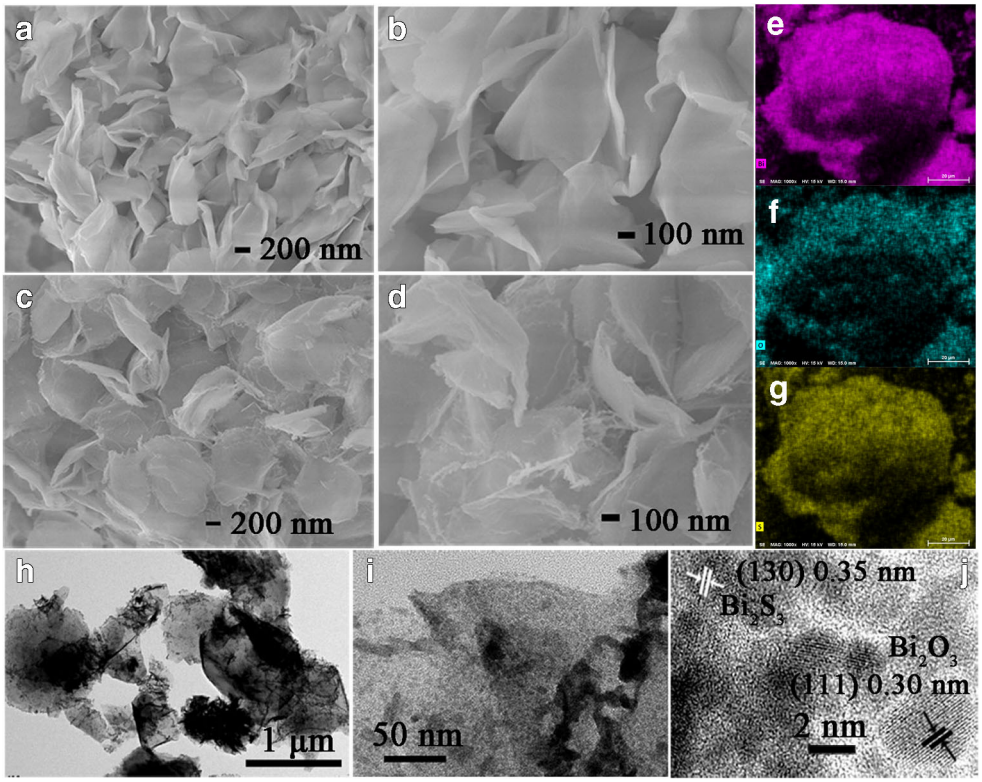

Fig. 1 FESEM images of Bi_2O_3 (**a**, **b**) and Bi_2S_3@Bi_2O_3 heterojunction (**c**, **d**). The elemental mappings are shown for the Bi (**e**), O (**f**), and S (**g**). TEM images (**h**, **i**) and HRTEM image (**j**) for the Bi_2S_3@Bi_2O_3 heterojunction

rough and wrinkled after the introduction of sulfurizing reagent. The high-magnification image in Fig. 1 D also demonstrates that the surfaces of Bi_2S_3@Bi_2O_3 are wrinkled. To further confirm the composition of the obtained Bi_2S_3@Bi_2O_3 nanosheets, the corresponding elemental mappings were tested. As shown in Fig. 1 E–G, the co-presence and homodisperse of Bi, O, and S elements in the nanosheets can be proved. The samples of Bi_2S_3@Bi_2O_3 were further conducted using TEM tests, and the wrinkles can be recognized clearly on the Bi_2S_3@Bi_2O_3 surface (Fig. 1H). The high-magnification image in Fig. 1 I also shows the feature of Bi_2S_3@Bi_2O_3 nanosheets, in which the Bi_2O_3 displays brighter color while the Bi_2S_3 presents darker color by contrast. The TEM image of the used GNPs demonstrates that they are spherical particles with the size of ~ 13 nm (see EMS Fig. S2). Figure 1 J illustrates that the atomic spacing of 0.35 nm corresponds to the (130) plane of Bi_2S_3, while the atomic spacing of 0.30 nm correlates with the (111) plane of Bi_2O_3. The results above indicate that the prepared Bi_2S_3@Bi_2O_3 sample owns a lamellar-like structure and the unique morphology, which can prove its application prospect in photoelectric chemistry. The patterns of as-synthesized Bi_2O_3 and Bi_2S_3@Bi_2O_3 nanosheets were also characterized using X-ray diffraction (XRD) spectra. Figure 2 A shows that all the diffraction peaks of the Bi_2O_3 nanosheets can be indexed to the cubic phase Bi_2O_3 according to JCPDS card no. 052-1007, and the major peaks have been marked by a circular shape. The major peaks of Bi_2O_3 show weak intensity, indicating the low crystallinity of the prepared Bi_2O_3. This phenomenon is completely consistent with the reported literature, because the cubic phase of Bi_2O_3 with high crystallization is hard to be obtained without further heat treated and annealed process [40]. The XRD pattern of the Bi_2S_3@Bi_2O_3 nanosheets agrees well with that of the bare Bi_2O_3, suggesting that there was no spoilage to Bi_2O_3 nanosheets with the introduction of Bi_2S_3. In addition, for the heterojunction of Bi_2S_3@Bi_2O_3, the peaks of Bi_2O_3 still exist. Simultaneously, new diffraction peaks appear corresponding to the orthorhombic phase Bi_2S_3, which are in accordance with the JCPDS card no. 17-0320. The results indicate the successful synthesis of Bi_2O_3 and Bi_2S_3@Bi_2O_3 nanosheets. In order to prove the composition of the prepared sample, X-ray photoelectron spectroscopy (XPS) measurements of Bi_2O_3 and Bi_2S_3@Bi_2O_3 sample were conducted. As shown in Fig. 2 B, the typical XPS survey spectrum illustrates that the Bi_2O_3 sample is composed of Bi and O elements, indicating the purity of Bi_2O_3. After moderate sulfurization, the characteristic peak located at 224.6 eV belongs to the S 2s peak [41], indicating the existence of S. The high-resolution Bi_2S_3@Bi_2O_3 and Bi_2O_3 XPS spectra are exhibited in Fig. 2 C and D, respectively. For Bi_2O_3, the peaks at binding energy of 164.4 and 159.1 eV present the spin-orbit splitting signals of Bi $4f_{7/2}$ and Bi $4f_{5/2}$, respectively. By way of comparison, two peaks of Bi_2S_3@Bi_2O_3 located at 159.8 and 165.1 eV are corresponding to Bi $4f_{5/2}$ and Bi $4f_{7/2}$, respectively. What is more, the Bi $4f_{7/2}$ and Bi $4f_{5/2}$ peaks for Bi_2S_3@Bi_2O_3 intend

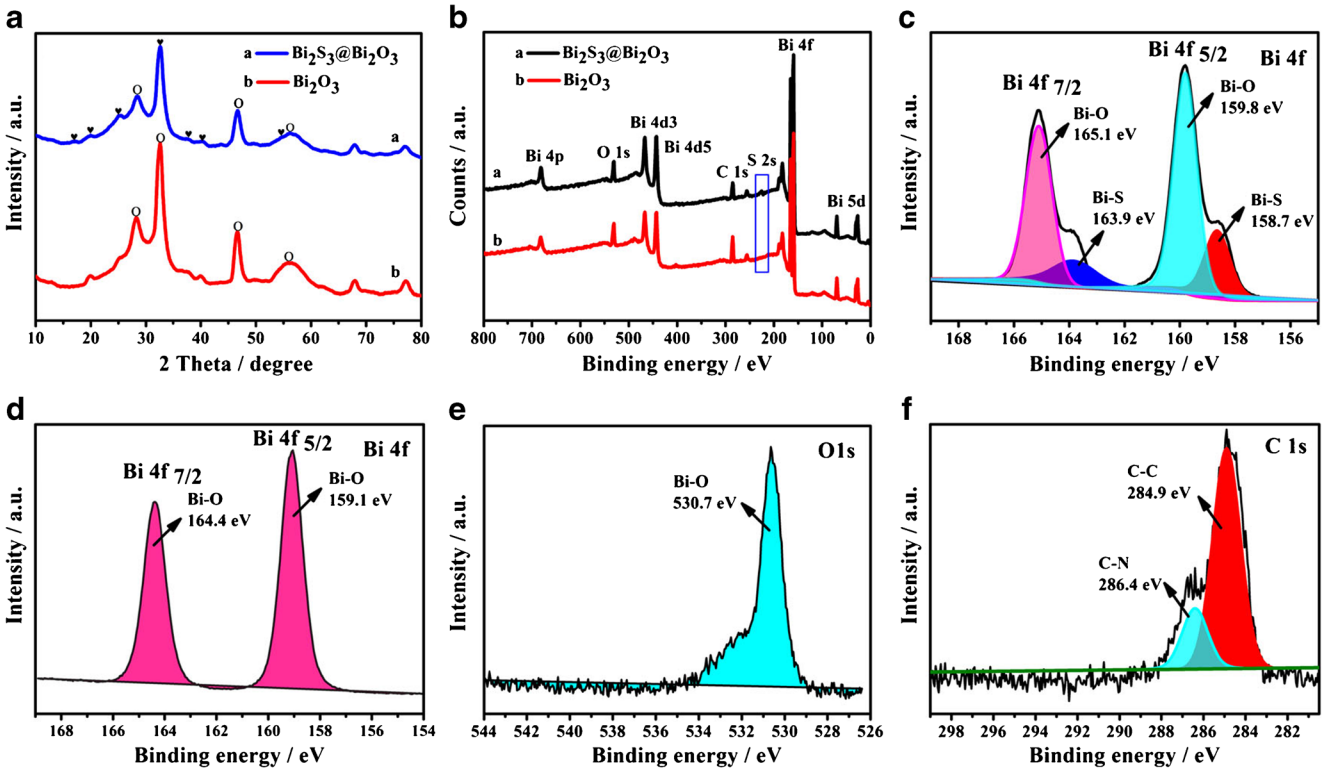

Fig. 2 (**a**) XRD patterns simulated from the X-ray crystal diffraction file for the as-prepared Bi_2S_3@Bi_2O_3 and Bi_2O_3. XPS analysis of (**b**) the full region for Bi_2S_3@Bi_2O_3 and Bi_2O_3, (**c**) Bi 4f region (for Bi_2S_3@Bi_2O_3), (**d**) Bi 4f region (for Bi_2O_3), (**e**) O 1s region, and (**f**) C 1s region

to shift about 0.7 eV toward lower energy, which can be ascribed to the coupling effect contributing to the forceful chemical bonding between the two compounds [42]. In addition, Fig. 2 E and F show the high-resolution spectra of O 1s and C 1s regions, respectively, for Bi_2S_3@Bi_2O_3. The peaks located at 530.7, 284.9, and 286.4 eV are assigned to the absorbed species, such as CTAB and H_2O. All of the results confirm that cubic Bi_2O_3 and orthorhombic Bi_2S_3 coexist in the Bi_2S_3@Bi_2O_3 nanosheets.

Photoelectrochemical property of Bi_2S_3@Bi_2O_3, Bi_2O_3, and Bi_2S_3 nanosheets

The optical properties of the synthesized Bi_2S_3@Bi_2O_3, Bi_2O_3, and Bi_2S_3 nanosheets were studied using the UV-vis diffuse reflectance spectroscopy. As displayed in Fig. 3 A, the Bi_2S_3 and Bi_2S_3@Bi_2O_3 have the similar wide absorption spectra, suggesting that they can absorb photons in the full spectrum of UV and visible light, whereas the absorption edge of Bi_2O_3 is at around 420 nm, showing its weak visible light absorption. Figure 3 B presents the corresponding band gap energies achieved according to the Tauc equation [43],

$$\alpha h\nu = A\left(h\nu - E_g\right)^n \tag{1}$$

where A in this equation is the material related constant, h denotes Planck's constant, ν is the light frequency, α represents the absorption coefficient, and E_g is the band gap. The value of n depends on the property of the semiconductor. The n is 0.5 for a direct semiconductor and equals to 2 for an indirect semiconductor. We can clearly learn that the relationship between $(\alpha h\nu)^{1/2}$ and $h\nu$ represents the linear relation for indirect transitions; nevertheless, the relation of $(\alpha h\nu)^2$ versus $h\nu$ denotes the linearity for direct transitions in the absorption edge region [44]. Figure 3 B displays the Tauc equation of $(\alpha h\nu)^2$ versus $h\nu$ for Bi_2S_3@Bi_2O_3, Bi_2O_3, and Bi_2S_3 nanosheets and demonstrates a good linearity in the absorption edge region. This result demonstrates the direct transitions for Bi_2S_3@Bi_2O_3, Bi_2O_3, and Bi_2S_3 nanosheets in the absorption edge region, respectively. The band gap energies, E_g, of Bi_2S_3@Bi_2O_3, Bi_2O_3, and Bi_2S_3 nanosheets are calculated to be 1.7, 3.0, and 1.3 eV, respectively. Furthermore, the band positions of conduction band (CB) and valence band (VB) of the prepared Bi_2S_3@Bi_2O_3, Bi_2O_3, and Bi_2S_3 at the point of zero charge were predicted using the empirical equations listed below,

$$E_{CB} = \chi - E^C - 0.5\,E_g, \tag{2}$$

$$E_{VB} = E_{CB} + E_g, \tag{3}$$

where χ and E^C denote the absolute electronegativity of the semiconductor and the energy of free electrons on the hydrogen scale (approximately 4.5 eV), respectively; for the compound of $A_aB_bC_c$, which is composed of elements A, B, and C

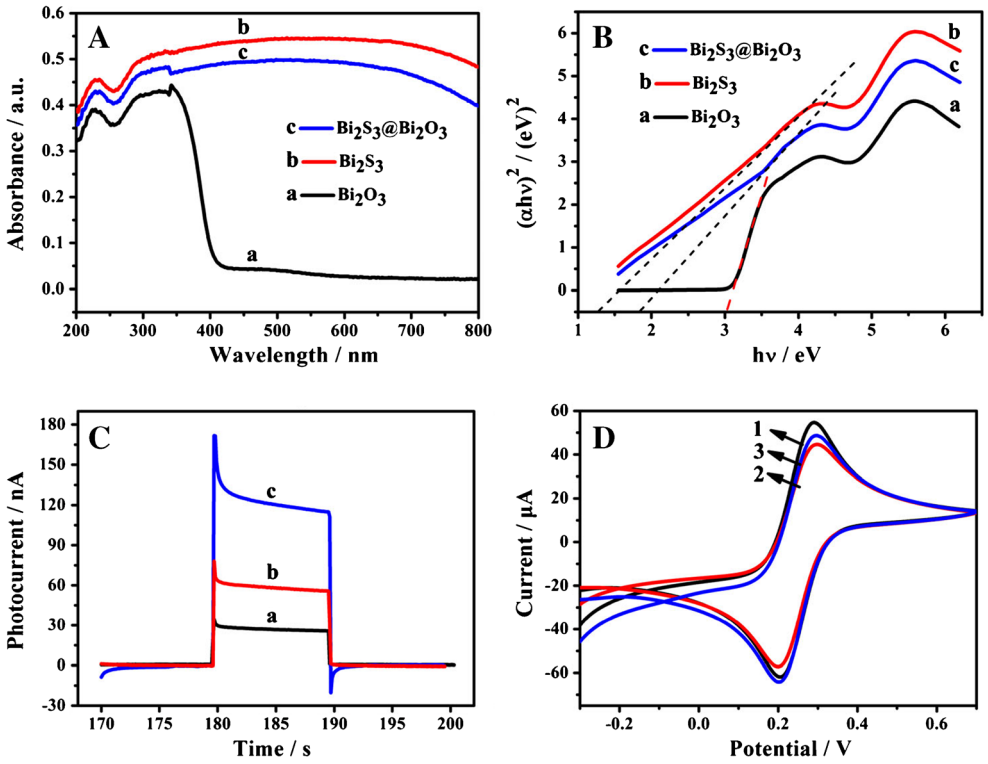

Fig. 3 (**A**) UV-vis diffuse reflectance spectra and (**B**) Tauc's plots of the Bi_2O_3, Bi_2S_3, and Bi_2S_3@Bi_2O_3. (**C**) Photocurrent intensity for the designed sensor of (**a**) Bi_2O_3/GCE, (**b**) Bi_2S_3/GCE, and (**c**) Bi_2S_3@Bi_2O_3/GCE. (**D**) CV profiles in $[Fe(CN)_6]^{3-/4-}$ solution (5.0 mM) for the (1) GCE, (2) Bi_2S_3@Bi_2O_3/GCE, and (3) GNPs/Bi_2S_3@Bi_2O_3/GCE

(*a*, *b*, and *c* represent the number of atoms that consist of the compound),

$$\chi = \left(\chi(A)^a \chi(B)^b \chi(C)^c\right)^{1/(a+b+c)} \quad (4)$$

The calculated results of E_{CB} and E_{VB} for Bi_2O_3 are approximately 0.23 and 3.23 eV, and for Bi_2S_3 are calculated to be approximately 0.12 and 1.42 eV. The χ value for Bi_2S_3 and Bi_2O_3 is 5.27 and 6.23, respectively (see ESM Table S1). From the above results, the possible photoexcited electron hole processes over Bi_2S_3@Bi_2O_3 under visible light irradiation are proposed in Scheme 2, ever since the band-edge potential levels are playing a significant role in improving the progress of photoexcited electron hole pairs in the photoactive material. In detail, when the PEC electrode is excited by white light, both Bi_2S_3 and Bi_2O_3 are easy to be excited under white light irradiation. Ultimately, photoexcited electrons and holes are produced in VB and CB of samples, respectively. The photo-induced electrons are transferred with high efficiency from CB of Bi_2S_3 to CB of Bi_2O_3 owing to the construction of heterogeneous junction of the semiconductors of Bi_2S_3 and Bi_2O_3. Meanwhile, photo-generated holes on the VB of Bi_2O_3 can be migrated to Bi_2S_3 under the band energy potential difference. As a result, the hole from Bi_2S_3 oxidizes the target analyte L-Cys. Thus, the designed Bi_2S_3@Bi_2O_3 heterojunction nanosheets would accelerate the electron transfer and then amplify the photocurrent response. Figure 3 C shows the photocurrent response of pure Bi_2O_3 (curve a) and Bi_2S_3 (curve b), respectively. After forming a heterogeneous structure between Bi_2S_3 and Bi_2O_3, the photocurrent signal presented three times and four times higher than that of Bi_2S_3 and Bi_2O_3. The result indicated that the formed Bi_2S_3@Bi_2O_3 heterojunction structure can improve the photocurrent response of the Bi_2S_3@Bi_2O_3/GCE (curve c) electrode obviously due to the higher separation efficiency of the

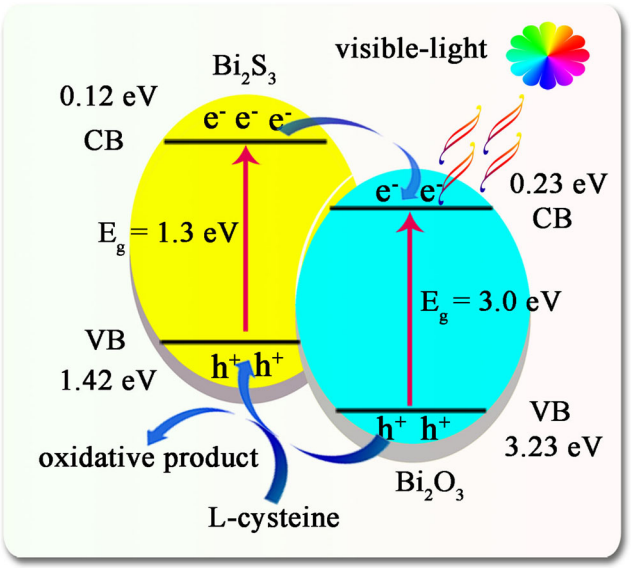

Scheme 2 Schematic diagram of the PEC reaction mechanism based on the Bi_2S_3@Bi_2O_3 heterojunction

photoexcited electron hole pairs in the Bi_2S_3@Bi_2O_3 nanosheets. To prove the successful construction of the modified electrode in the stepwise modification process, the cyclic voltammetry (CV) was used to investigate the stepwise-modified electrode. As shown in Fig. 3 D, it can be observed that there is a pair of reversible redox peaks for the GCE (curve 1), after the Bi_2S_3@Bi_2O_3 nanosheet was modified on the surface of the GCE (curve 2), the obtained peak current obviously decreased. When GNPs were incubated on the electrode, the oxidation reduction peak current increased obviously, indicating that GNPs have a good conductivity and provide a large surface area to facilitate electron transfer (curve 3). In addition, to assess the electrochemical active surface area (ECSA) of the working electrode, double-layer capacitance (C_{dl}) of the substrate was also measured by a simple CV method to roughly calculate the value of ECSA (see ESM Fig. S3), which is around 0.17 cm^2.

Optimum conditions for the detection of L-Cys

In order to obtain an optimal analytical performance, the related experiment conditions were discussed (the experimental details are shown in the supporting material). In the sensor building process, the concentration of Bi_2S_3@Bi_2O_3, the covering amount of Bi_2S_3@Bi_2O_3, and the bias potential can affect the PEC signal for the target analyte. The influence of Bi_2S_3@Bi_2O_3 concentration on the constructed sensor toward L-Cys (see ESM Fig. S4A) illustrates clearly that the photocurrent signal improved gradually with increasing the Bi_2S_3@Bi_2O_3 concentration between 1.0 and 1.5 mg/mL, and gets the maximum at 1.5 mg/mL. However, after the Bi_2S_3@Bi_2O_3 level exceeds 1.5 mg/mL, the photocurrent signal was decreased. The reason is that the thickness of the Bi_2S_3@Bi_2O_3 film is thin, which can improve the electron transfer resistance. Hence, 1.5 mg/mL Bi_2S_3@Bi_2O_3 was chosen as the optimum condition.

The influence of the amount of Bi_2S_3@Bi_2O_3 coating was also investigated. The polished bare GCE was dipped into different volumes of 1.5 mg/mL Bi_2S_3@Bi_2O_3 nanosheets (3, 5, 7, 9, 11 μL) and evaporated in air, and the photocurrent response was then recorded. The photocurrent signal increases with increasing coating amount before 7 μL, and decreased after it exceeds this value (see ESM Fig. S4B). In consequence, 7 μL of Bi_2S_3@Bi_2O_3 nanosheets was selected as the optimal coating amount for subsequent L-Cys assay.

In addition, as a significant factor in the PEC sensing system, the effect of the applied bias potential on the PEC sensor was studied (see ESM Fig. S4C). The photocurrent intensity declines with increasing the bias potential from − 0.2 to 0 V, while the photocurrent increases at the range of 0 to 0.2 V, suggesting that more positive potential drives more photogenerated electrons to the working electrode for the reduction of electron acceptor. In addition, in order to avoid large background current in the dark and minimize the electrochemical stress of the Bi_2S_3@Bi_2O_3 on the electrode under a given light intensity, the applied bias potential is 0.2 V in this study.

The corresponding calibration curve for the determination of L-Cys

To achieve the performance of the sensing in the determination of L-Cys (0.1–10,000 μM), the periodic photoresponse contained the fast separation, slow decay, steady state, and fast recombination PEC processes, which can also realize the high electron separation and transfer. Under the optimized conditions, the relationship between L-Cys concentration and photocurrent signal was studied. After loading onto the substrate, the L-Cys was sensitively analyzed. As displayed in Fig. 4 A, the photocurrent response improves with the increase of L-Cys concentration. Figure 4 B shows that over a concentration range of 0.1 to 10,000 μM, a plot of the photocurrent signal as a function of L-Cys concentration is linear. The corresponding linear regression equation is i (nA) = 20.35 log c (μM) + 160.37 (R^2 = 0.997) with a low limit of detection (LOD) of 0.07 μM for L-Cys, which was calculated in terms of the $3\sigma/s$, where s is the slope of the calibration plot and σ the standard deviation of the blank solution. The data in the calibration curve came from the values obtained at the midpoint of the photocurrent curves. As the concentration increases, the current value increases gradually, which indicates an excellent sensing performance with the ultralow LOD and a wider linear range compared with published articles (see ESM Table S2). There are several factors contributing to the well-performed sensor: (1) the outstanding photoactive material of Bi_2S_3@Bi_2O_3 nanosheets and good conductive collosol of Au; (2) the designed process is clever, concise, and operable; (3) the presence of L-Cys in the electrolyte solution can effectively promote the separation of electron hole pairs.

Selectivity, stability, and repeatability of the prepared biosensor

In order to monitor the selectivity of the prepared sensor, the amino acids including L-Arg, L-Pro, L-Ala, L-His, L-Try, L-Leu, L-Thr, L-Ser, l-Glu, and L-Cys were studied by replacing L-Cys with 200 μM above amino acids under the same experimental conditions, respectively. In addition, GSH, a biologically important thiol compound, was also investigated to further evaluate the selectivity. As displayed in Fig. 4 C, the amino acids such as L-Arg, L-Pro, L-Ala, L-His, L-Try, L-Leu, L-Thr, L-Ser, and L-Glu have negligible photocurrent response on the prepared PEC sensor because there is no SH group in these amino acids to form the bond of Au-S. However, GSH has slight effect on the measurement of L-Cys due to the SH group. These results indicate the good specificity of the designed PEC sensor.

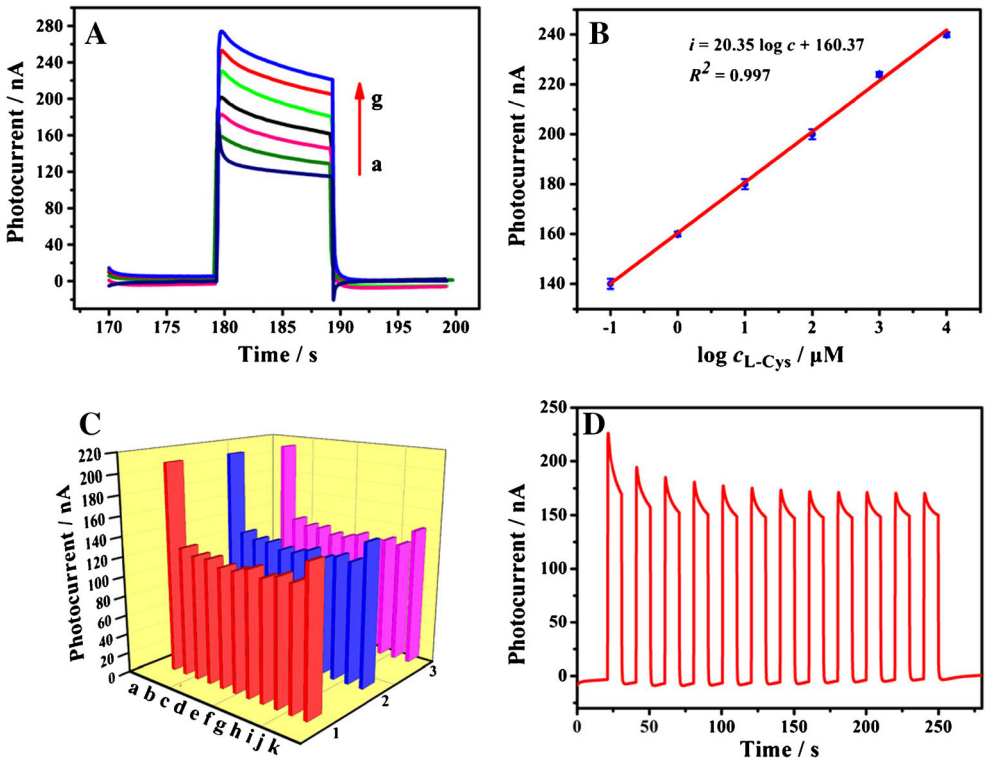

Fig. 4 (**A**) PEC signals of the designed sensor in Na_2SO_4 solution (0.1 M). L-Cys concentration (from (**a**) to (**g**), μM): 0, 0.1, 1, 10, 100, 1000, and 10,000. (**B**) The corresponding calibration curve for the determination of L-Cys. (**C**) Selectivity of the PEC sensing toward other interfering substances. (**a**)–(**k**) The foreign substances (200 μM) of L-Cys, L-Arg, L-Pro, L-Ala, L-His, L-Try, L-Leu, L-Thr, L-Ser, L-Glu, and GSH, respectively. The numbers 1, 2, and 3 represent the serial number of each experimental measurement, respectively. (**D**) Photocurrent intensity of the constructed sensing after scanning for 10 cycles, and the related L-Cys level is 1 μM

The PEC signal was conducted under light on and off irradiation cycles (Fig. 4D) and no significant change can be observed, suggesting the steady reading for signal collection. Furthermore, the repeatability was estimated on the basis of the within-batch precision and between-batch precision. The related electrode reacted with 1 μM L-Cys is repeated six times, and the within-batch relative standard deviation (RSD) is 5.6% and the between-batch RSD is 4.3% obtained from six incubated electrodes. The results indicate the acceptable repeatability of the resulting sensor. The photocurrent response of the constructed electrodes reduces by 8.6% when stored for over 1 month. The result mentioned above shows a good storage stability of Bi_2S_3@Bi_2O_3 nanosheets and the excellent repeatability can also be found in the developed PEC sensing.

Application in real samples

To further study the application potential and the analytical reliability of our assay in real samples, the concentrations of L-Cys in human urine collected from healthy volunteers were detected via the proposed strategy, and the recovery experiments were measured through the L-Cys-spiked human urine. The recovery varies from 90.0 to 104.0% and the RSD is 4.3–5.8% (see ESM Table S3); these assayed results demonstrated that the developed method possesses a good practicability for the determination of L-Cys in real samples.

Conclusion

In summary, Bi_2O_3@Bi_2S_3 heterojunction has been synthesized using the one-step water bath method. The heterojunction photoactive material presents significantly improved PEC performance in the detection of L-Cys assay under the irradiation of visible light, which is superior to the pure Bi_2S_3 or Bi_2O_3. On account of the estimated energy band edges, the mechanism of improved PEC response for the prepared heterojunction has been investigated in detail. The improved PEC performance stems from the effective separation of electron hole pairs, which is derived from the formation of heterojunction between the semiconductors of Bi_2O_3 and Bi_2S_3. Furthermore, the successfully developed sensing system has a highly specific response and lower detection limit, thus exhibiting an outstanding analytical performance in L-Cys detection. Therefore, this heterojunction is promising in early biomedical research and clinical diagnostics.

Acknowledgments This work received financial support from the National Natural Science Foundation of China (No. 21675131), the Natural Science Foundation of Chongqing (No. CSTC-2015jcyjB50001), and the Fundamental Research Funds for the Central Universities of China (SWU 114089 and XDJK 2014C136).

Compliance with ethical standards The study was approved by the Ethics Committee of Southwest University, and written informed consent was obtained from all individuals participating in the study prior to the collection of the human urine samples.

Conflict of interest The authors declare that they have no competing interests.

References

1. Zhu YH, Xu ZW, Yan K, Zhao HB, Zhang JD. One-step synthesis of CuO–Cu_2O heterojunction by flame spray pyrolysis for cathodic photoelectrochemical sensing of L-cysteine. ACS Appl Mater Interfaces. 2017;9:40452–60.
2. Shahrokhian S. Lead phthalocyanine as a selective carrier for preparation of a cysteine-selective electrode. Anal Chem. 2001;73(24):5972–8.
3. Chwatko G, Bald E. Silver nanoparticles in the presence of Ca^{2+} as a selective and sensitive probe for the colorimetric detection of cysteine. Talanta. 2000;52(3):509–15.
4. Ayaz Ahmed KB, Sengan M, Kumar PS, Veerappan A. Highly selective colorimetric cysteine sensor based on the formation of cysteine layer on copper nanoparticles. Sensors Actuators B Chem. 2016;233:431–7.
5. Hua L, Han H, Zhang X. Size-dependent electrochemiluminescence behavior of water-soluble CdTe quantum dots and selective sensing of L-cysteine. Talanta. 2009;77(5):1654–9.
6. Ozoemena K, Westbroek P, Nyokong T. Long-term stability of a gold electrode modified with a self-assembled monolayer of octabutylthiophthalocyaninato-cobalt (II) towards L-cysteine detection. Electrochem Commun. 2001;3(9):529–34.
7. Yang S, Li G, Wang Y, Wang G, Qu L. Amperometric L-cysteine sensor based on a carbon paste electrode modified with Y_2O_3 nanoparticles supported on nitrogen-doped reduced graphene oxide. Microchim Acta. 2016;183(4):1351–7.
8. Ye C, Wang MQ, Li LJ, Luo HQ, Li NB. Fabrication of Pt/$Cu_3(PO_4)_2$ ultrathin nanosheet heterostructure for photoelectrochemical microRNA sensing using novel G-wire-enhanced strategy. Nanoscale. 2017;9:7526–32.
9. Ye C, Wang MQ, Gao ZF, Zhang Y, Lei JL, Luo HQ, et al. Ligating dopamine as signal trigger onto the substrate via metal-catalyst-free click chemistry for "signal-on" photoelectrochemical sensing of ultralow microRNA levels. Anal Chem. 2016;88:11444–9.
10. Lv SZ, Zhang KY, Zeng YY, Tang DP. Double photosystems-based 'Z-Scheme' photoelectrochemical sensing mode for ultrasensitive detection of disease biomarker accompanying three-dimensional DNA walker. Anal Chem. 2018;90:7086–93.
11. Luo ZB, Zhang LJ, Zeng RJ, Su LS, Tang DP. Near-infrared light-excited Core–Core–Shell UCNP@Au@CdS upconversion nanospheres for ultrasensitive photoelectrochemical enzyme immunoassay. Anal Chem. 2018;90:9568–75.
12. Shu J, Tang DP. Current advances in quantum-dots-based photoelectrochemical immunoassays. Chem Asian J. 2017;12:2780–9.
13. Zhao WW, Xu JJ, Chen HY. Photoelectrochemical bioanalysis: the state of the art. Chem Soc Rev. 2015;44:729–41.
14. Zhao W, Ma Z, Yu P, Dong X, Xu J, Chen H. Highly sensitive photoelectrochemical immunoassay with enhanced amplification using horseradish peroxidase induced biocatalytic precipitation on a CdS quantum dots multilayer electrode. Anal Chem. 2011;84:917–23.
15. Huo H, Xu Z, Zhang T, Xu C. Ni/CdS/TiO_2 nanotube array heterostructures for high performance photoelectrochemical biosensing. J Mater Chem A. 2015;3:5882–8.
16. Wang FX, Ye C, Mo S, Liao LL, Zhang XF, Ling Y, et al. A novel "signal-on" photoelectrochemical sensing for ultrasensitive detection of alkaline phosphatase activity based on TiO_2/g-C_3N_4 heterojunction. Analyst. 2018;143:3399–407.
17. Kment S, Riboni F, Pausova S, Wang L, Wang L, Han H, et al. Photoanodes based on TiO_2 and α-Fe_2O_3 for solar water splitting–superior role of 1D nanoarchitectures and of combined heterostructures. Chem Soc Rev. 2017;46:3716–69.
18. Zhang Y, Hao N, Zhou Z, Hua R, Qian J, Liu Q, et al. A potentiometric resolved ratiometric photoelectrochemical aptasensor. Chem Commun. 2017;53:5810–3.
19. Wang X, Blechert S, Antonietti M. Polymeric graphitic carbon nitride for heterogeneous photocatalysis. ACS Catal. 2012;28:1596–606.
20. Wang Y, Hao N, Feng Q, Shi H, Xu J, Chen H. A ratiometric electrochemiluminescence detection for cancer cells using g-C_3N_4 nanosheets and Ag–PAMAM–luminol nanocomposites. Biosens Bioelectron. 2016;77:76–82.
21. Li X, Zhang X, Ma H, Wu D, Zhang Y, Du B, et al. Cathodic electrochemiluminescence immunosensor based on nanocomposites of semiconductor carboxylated g-C_3N_4 and graphene for the ultrasensitive detection of squamous cell carcinoma antigen. Biosens Bioelectron. 2014;55:330–6.
22. Zhuang JY, Lai WQ, Xu MD, Zhou Q, Tang DP. Plasmonic AuNP/g-C_3N_4 nanohybrid-based photoelectrochemical sensing platform for ultrasensitive monitoring of polynucleotide kinase activity accompanying DNAzyme-catalyzed precipitation amplification. ACS Appl Mater Interfaces. 2015;7:8330–8.
23. Lim H, Lee J, Jin S, Kim J, Yoon J, Hyeon T. Highly active heterogeneous Fenton catalyst using iron oxide nanoparticles immobilized in alumina coated mesoporous silica. Chem Commun. 2006;4:463–5.
24. Sun W, Zhang H, Lin J. Surface modification of Bi_2O_3 with Fe(III) clusters toward efficient photocatalysis in a broader visible light region: implications of the interfacial charge transfer. J Phys Chem C. 2014;118:17626–32.
25. Muruganandham M, Amutha R, Lee G, Hsieh S, Wu J, Sillanpaa M. Facile fabrication of tunable Bi_2O_3 self-assembly and its visible light photocatalytic activity. J Phys Chem C. 2012;116:12906–15.
26. Lai CF, Chang CC, Wen MH, Lin CK, Wu MK. Enhanced efficiency in InGaN-based photovoltaic devices combined with nanocrystalline Bi_2O_3/P3HT heterojunction structures. Phys Status Solidi A. 2013;210:1133–6.
27. Park S, Kim S, Sun GJ, Lee C. Synthesis, structure, and ethanol gas sensing properties of In_2O_3 nanorods decorated with Bi_2O_3 nanoparticles. ACS Appl Mater Interfaces. 2015;7:8138–46.
28. Xie T, Liu C, Xu L, Yang J, Zhou W. Novel heterojunction Bi_2O_3/$SrFe_{12}O_{19}$ magnetic photocatalyst with highly enhanced photocatalytic activity. J Phys Chem C. 2013;117:24601–10.
29. Lee C, Jeong S, Myung N, Rajeshwar K. Preparation of Au-Bi_2O_3 nanocomposite by anodic electrodeposition combined with galvanic replacement. J Electrochem Soc. 2014;161:499–503.
30. Meng F, Li J, Cushing SK, Zhi M, Wu N. Solar hydrogen generation by nanoscale *p–n* junction of *p*-type molybdenum disulfide/*n*-type nitrogen-doped reduced graphene oxide. J Am Chem Soc. 2013;135:10286–9.
31. Wang H, Zhang L, Chen Z, Hu J, Li S, Wang Z, et al. Semiconductor heterojunction photocatalysts: design, construction, and photocatalytic performances. Chem Soc Rev. 2014;43:5234–44.
32. Li H, Zhou Y, Tu W, Ye J, Zou Z. State-of-the-art progress in diverse heterostructured photocatalysts toward promoting photocatalytic performance. Adv Funct Mater. 2015;25:998–1013.
33. Wang M, Sun L, Lin Z, Cai J, Xie K, Lin C. p-n Heterojunction photoelectrodes composed of Cu_2O-loaded TiO_2 nanotube arrays with enhanced photoelectrochemical and photoelectrocatalytic activities. Energy Environ Sci. 2013;6:1211–20.
34. Vogel R, Hoyer P, Weller HJ. Quantum-sized PbS, CdS, Ag_2S, Sb_2S_3, and Bi_2S_3 particles as sensitizers for various nanoporous wide-bandgap semiconductors. J Phys Chem. 1994;98:3183–8.

35. Zhang B, Ye XC, Hou WY, Zhao Y, Xie Y. Biomolecule-assisted synthesis and electrochemical hydrogen storage of Bi_2S_3 flowerlike patterns with well-aligned nanorods. J Phys Chem B. 2006;110(18): 8978–85.
36. Bao HF, Li CM, Cui XQ, Gan Y, Song QL, Guo J. Bi_2S_3 nanostructures: a new photocatalyst. Small. 2008;4:1125–9.
37. Yao K, Gong WW, Hu YF, Liang XL, Chen Q, Peng LM. Individual Bi_2S_3 nanowire-based room-temperature H_2 sensor. J Phys Chem C. 2008;112:8721–4.
38. Luo Y, Chen H, Li X, Gong X, Wang X, Peng X, et al. Wet chemicalsynthesis of Bi_2S_3 nanorods for efficient photocatalysis. J Mater Lett. 2013;105:12–5.
39. Luo W, Li F, Li QD, Wang XP, Yang W, Zhou L, et al. Heterostructured Bi_2S_3-Bi_2O_3 nanosheets with a built-in electric field for improved sodium storage. ACS Appl Mater Interfaces. 2018;10:7201–7.
40. Deng Z, Liu T, Chen T, Jiang J, Yang W, Guo J, et al. Enhanced electrochemical performances of Bi_2O_3/rGO nanocomposite via chemical bonding as anode materials for lithium ion batteries. ACS Appl Mater Interfaces. 2017;9:12469–77.
41. Tian L, Tan HY, Vittal JJ. Morphology-controlled synthesis of Bi_2S_3 nanomaterials via single- and multiple-source approaches. Cryst Growth Des. 2007;8:734–8.
42. Gao MR, Yu SH, Yuan J, Zhang W, Antonietti M. Poly (ionic liquid)-mediated morphogenesis of bismuth sulfide with a tunable band gap and enhanced electrocatalytic properties. Angew Chem Int Ed. 2016;128:13004–8.
43. Ke J, Liu J, Sun HQ, Zhang HY, Duan XG, Liang P, et al. Facile assembly of Bi_2O_3/Bi_2S_3/MoS_2 np heterojunction with layered n-Bi_2O_3 and p-MoS_2 for enhanced photocatalytic water oxidation and pollutant degradation. Appl Catal B Environ. 2017;200:47–55.
44. Zhang JJ, Wang T, Chang XX, Li A, Gong JL. Fabrication of porous nanoflake $BiMO_x$ (M = W, V, and Mo) photoanodes via hydrothermal anion exchange. Chem Sci. 2016;7:6381–6.